RSC Sustainability

ROYAL SOCIETY OF CHEMISTRY

PAPER

View Article Online
View Journal | View Issue



Cite this: *RSC Sustainability*, 2024, **2**, 3424

# $Ti_3C_2T_x$ MXene coupled $Co(OH)_2$: a stable electrocatalyst for the hydrogen evolution reaction in alkaline media

Muhammad Yameen Solangi,[a] Aashiq Ali Lakhair,[a] Farkhanda Zaman Dayo,[b] Rehan Ali Qureshi,[a] Abdulaziz Alhazaa,[c] Muhammad Ali Shar,[d] Abdul Jalil Laghari,[a] Imtiaz Ali Soomro,[a] Muhammad Nazim Lakhan,[e] Abdul Hanan *[f] and Umair Aftab *[a]

Green hydrogen ($H_2$) production *via* water electrolysis is a promising technique. Within this domain, two dimensional (2D) materials are gaining more attention throughout the world particularly in energy conversion/storage devices due to their unique features. Herein, this study focuses on the development of sustainable, durable, and economical electrocatalysts based on titanium carbide ($Ti_3C_2T_x$) MXene and cobalt hydroxide ($Co(OH)_2$) as a composite. $Ti_3C_2T_x$ has been doped into $Co(OH)_2$ (CT nanostructure) with varying concentrations by the aqueous chemical growth method. The as-prepared electrocatalysts (CT-15 and CT-30) have been investigated through different physicochemical characterization studies including X-ray diffraction (XRD), scanning electron microscopy (SEM), Fourier transform infrared spectroscopy (FTIR), and electrochemical analysis in order to access their morphology, crystalline phase homogeneity, surface functionalization, and electrochemical behaviour for the HER. It is observed that the as-prepared material (CT-30) exhibits superior hydrogen evolution reaction (HER) activity in 1.0 M potassium hydroxide (KOH). The optimised electrocatalyst CT-30 demonstrates an overpotential of 380 mV at a current density of 10 mA $cm^{-2}$ with a 99 mV $dec^{-1}$ Tafel slope value, showing fast reaction kinetics. Moreover, it offers a low charge transfer resistance ($R_{ct}$) accompanied by good stability, high electrochemical active surface area (ECSA), and durability for 30 h, as evident for efficient HER activity. This novel electrocatalyst can contribute to the replacement of noble metal-based electrocatalysts for practical usage in energy conversion/storage systems.

Received 23rd July 2024
Accepted 18th September 2024

DOI: 10.1039/d4su00392f

rsc.li/rscsus



## Sustainability spotlight

Combining $Ti_3C_2T_x$ (MXene) with $Co(OH)_2$ as an electrocatalyst for the hydrogen evolution reaction (HER) in an alkaline medium improves both the effectiveness and long-term stability of the catalytic process, while also making a substantial contribution to sustainability. This sophisticated electrocatalyst contributes to the achievement of Sustainable Development Goal (SDG) 7 by facilitating the generation of economical and environmentally friendly energy *via* enhanced hydrogen ($H_2$) production, which is crucial for the advancement of renewable energy technology. Additionally, by promoting cleaner energy alternatives, it also contributes to achieving Sustainable Development Goal 13 by lessening the negative effects of climate change *via* decreased dependence on fossil fuels and decreased emissions of greenhouse gases. Hence, the incorporation of $Co(OH)_2$ into $Ti_3C_2T_x$ as an electrocatalyst is a crucial method for attaining a long-lasting and robust energy future, directly contributing to worldwide sustainability goals.

## 1. Introduction

Demand for energy is increasing with the world population, so the annual consumption per capita is expected to increase with advancement in the human lifestyle.[1] Currently, fossil fuels account for 80% of the world's total energy production. However, the combustion of these fuels releases greenhouse gases into the atmosphere, leading to adverse effects on the climate. This, in turn, causes a rise in global temperatures and poses a threat to freshwater reserves.[2] It is the need of the world to invent more efficient and economical renewable energy

[a]*Department of Metallurgy and Materials Engineering, Mehran University of Engineering and Technology, Pakistan. E-mail: umair.aftab@faculty.muet.edu.pk*
[b]*Institute of Chemistry, Shah Abdul Latif University, Khairpur, Pakistan*
[c]*Department of Physics and Astronomy, College of Science, King Saud University, Riyadh, Saudi Arabia*
[d]*Department of Mechanical & Energy Systems Engineering, Faculty of Engineering and Informatics, University of Bradford, UK*
[e]*Applied Chemistry and Environmental Science, School of Science, STEM College, RMIT University, Melbourne, Australia*
[f]*Sunway Centre for Electrochemical Energy and Sustainable Technology (SCEEST), School of Engineering and Technology, Sunway University, Selangor, Malaysia. E-mail: ahanansamo@gmail.com*

sources.[3] Hydrogen ($H_2$) production technologies are gaining more attention as a renewable energy source in which the $H_2$ is produced by steam reforming, thermal decomposition, biomass fermentation, and electrolysis.[4–6] Among all these methods, the water electrolysis approach is more attractive due to producing $H_2$ from water molecules by splitting it into $H_2$ and oxygen ($O_2$). There are two kinds of reactions that occur during the water splitting process such as the hydrogen evolution reaction (HER) and oxygen evolution reaction (OER) in the process of electrolysis.[7,8] The HER and OER take place at the cathode and anode side in acidic and alkaline electrolytes, respectively. However, the HER offers more hindrances in an alkaline environment, so more electrical potential is required to carry out this reaction effectively.[9,10] In order to rectify this issue, noble metal-based electrocatalysts such as platinum (Pt), ruthenium (Ru) and iridium (Ir) and their alloys, are used to facilitate this reaction at low overpotential.[11,12] However, these noble catalysts are costly due to limited reserves leading to less economical output for mass scale production. Therefore, the world is focusing on alternative materials that are reliable for industrial scale $H_2$ production.[13]

For this reason, transition metal (TM)-based catalysts have been developed such as sulfides, carbides,[14,15] phosphides,[16,17] nitrides,[18] oxides,[19,20] and hydroxides.[21,22] From these reported catalysts, TM hydroxide-based catalysts offer good stability and efficient electrochemical performance. In addition, various metal hydride catalysts have been reported to enhance the HER activity, but cobalt-based hydroxides are most favourable due to their lowest possible reaction rate, tuneable electronic structure and morphological characteristics.[23] For example, X.-Y. Zhang *et al.*[24] reported CoFeOH encapsulated CoFeP on iron foam (CoFeOH/CoFeP/IF) for reducing phosphorus loss and enhancing its performance in alkaline media. Furthermore, X. Feng *et al.*[25] synthesized hollow nanotubes of Ni/CoFe hydroxide and Ni/$CoSe_2$ on nickel foam through the electrodeposition process to optimize the HER electrochemical reaction kinetics. Moreover, Zhan *et al.*[26] effectively generated a precursor material by electrodeposition of two doping elements to create a co-doped cobalt hydroxide electrocatalyst (Ru-Co$(OH)_2$-Se). This strategy has been shown to be an efficacious method for enhancing the performance of the HER. The test findings indicate that the material had a reduced impedance value and an increased electrochemically active surface area.

Previously, two-dimensional (2D) materials are developed and extensively used for energy storage and conversion applications.[27] Among them, MXenes are a novel material, which exhibit higher electrical conductivity and tuneable surface functionality.[28] MXenes can be prepared from the MAX phase having the general formula $M_{n+1}AX_n$ ($n$ = 1, 2, 3), where M represents TM, A denotes the IIIA or IVA elements and X shows nitrogen or carbon.[29,30] To produce MXenes, the A layer (Al, Ga, and so on) is selectively removed and terminated by $T_x$ functional groups (–O, –OH and –F). Mostly $Ti_3C_2T_x$ MXene is widely used in $H_2$ generation applications because of superior metallic conductivity and hydrophilicity.[31,32] Various thin layered MXene-based electrocatalysts have been recently reported in the literature for HER activity such as 1T/2H $MoS_2$ (25D)/$Ti_3C_2T_x$ −1,[33] Fe/Ni doped GO@$Ti_3C_2T_x$,[34] $MoS_2$/$Ti_3C_2$ (ref. 35), *etc.* Notwithstanding MXene's outstanding performance, a few issues remain, including low capacitance, weaker surface functional groups, unreacted microstructure, and restacking. Different approaches, including doping, surface modification, morphological control, and their hybrid composites with other TM materials, can be used to overcome these issues and improve the efficiency of energy conversion and storage devices.[35] In general, the doped MXene shows an increase in interlayer space and electrical conductivity. Selecting highly conductive carbon materials to couple with cobalt oxide, such as graphene, carbon nanotubes, and MXenes, has already been shown to be an effective way to increase catalytic behaviour by improving electrical conductivity.[36] Typically, carbon acts as a supporting matrix in various nanocomposites, boosting conductivity, preventing composite material aggregation, and increasing the material's specific surface area.[37]

In this study, a promising composite of $Ti_3C_2T_x$ and $Co(OH)_2$ has been prepared through the aqueous chemical growth method, wherein $Ti_3C_2T_x$ is doped into $Co(OH)_2$ nanostructures with varying concentrations such as 15 and 30 mg (CT-15 and CT-30). The structural, compositional, and morphological characteristics were also examined using various physico-chemical techniques. The as-prepared composites along with pristine materials were analysed for HER activity in 1.0 M KOH. The optimised composite CT-30 exhibits superior electrochemical performance with an overpotential of 380 mV at 10 mA $cm^{-2}$ current density, a Tafel slope of 99 mV $dec^{-1}$, and stability for 30 h. This is an entirely new approach and has not been reported before (Fig. 1).

## 2. Materials and methods

### 2.1 Materials

Cobalt chloride hexahydrate ($CoCl_2 \cdot 6H_2O$), urea ($CH_4N_2O$), deionized (DI) water, MAX phase ($Ti_3AlC_2$), 5 wt% Nafion, potassium hydroxide (KOH), hydrochloric acid (HCl) and hydrofluoric acid (HF) were bought from Sigma Aldrich in Karachi, Pakistan. The tests used high-grade analytical substances without purification.

### 2.2 Synthesis method

The composite of $Ti_3C_2T_x$ and $Co(OH)_2$ was synthesized in two stages which include preparation of the MXene and its composite with $Co(OH)_2$. Initially, the preparation of $Ti_3C_2T_x$ ($T_x$ = –F) MXene was performed by the HF + HCl etching method, wherein the layer of Al was removed from the $Ti_3AlC_2$ MAX phase. Here, 0.5 g of bulk MAX was progressively introduced in a Teflon lined beaker having 60 mL of 20% aqueous HF + 5% HCl. The resultant $Ti_3AlC_2$ powder was agitated continuously at room temperature for 40 h using a Teflon-lined magnetic bar. The etching/removal of Al layers from the MAX precursor was then conducted. For removal of the excess acidity of solution, HF acidic solutions were centrifuged multiple times with D.I. water until their pH reaches ~7. $Ti_3C_2T_x$ was collected and dried in a vacuum oven (to avoid oxidation).

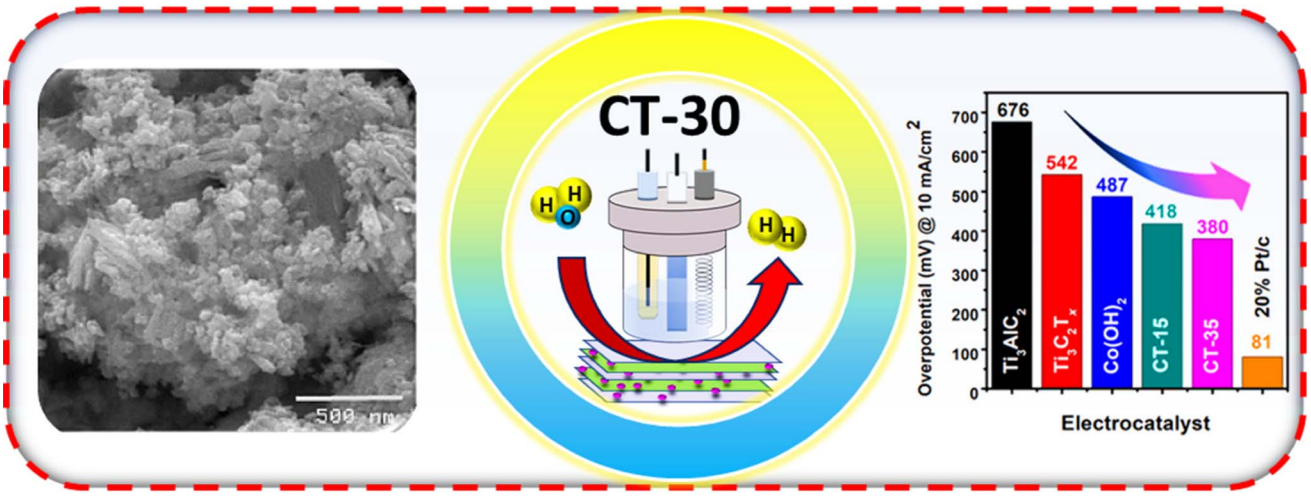


Fig. 1 The schematic illustration of this research study.

Secondly, the formation of the $Ti_3C_2T_x$ and $Co(OH)_2$ composite was conducted by the aqueous chemical growth method. Typically, 15 mg and 30 mg of prepared $Ti_3C_2T_x$ MXene were added individually into precursors of $Co(OH)_2$ and respectively labelled as CT-15 and CT-30. The precursors of $Co(OH)_2$ contained 0.1 M of $CoCl_2 \cdot 6H_2O$ and 0.1 M of $CH_4N_2O$ with the addition of $Ti_3C_2T_x$. The precursor solution was continually stirred on a magnetic stirrer until a homogenous solution was obtained and then placed in an electric oven at 95 °C for 5 h. After completing the growth time interval, the prepared composite was washed with DI water multiple times to remove other impurities. The samples were dried at room

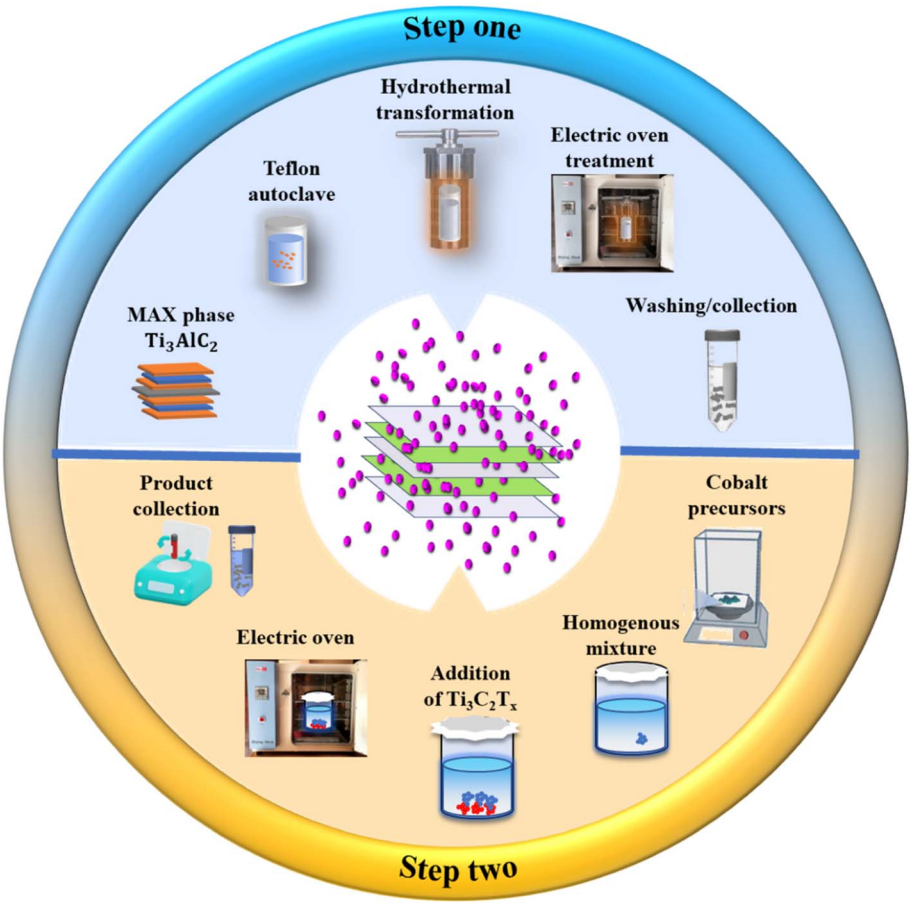


Fig. 2 Schematic illustration of the preparation of the $Ti_3C_2T_x$ MXene coupled $Co(OH)_2$ electrocatalyst.

temperature and collected in sample vials. In addition, pristine $Co(OH)_2$ was also synthesized similarly by following the above procedure (Fig. 2). Hence, as-synthesized $Ti_3C_2T_x$, $Co(OH)_2$, and $Ti_3C_2T_x$ doped $Co(OH)_2$ composites were ready to be characterized and optimized for electrochemical analysis.

### 2.3 Characterization

The X-ray diffraction (XRD) technique was conducted using a Philips PAN analytical X-ray diffractometer to evaluate the crystal orientation and phase purity of the prepared nanostructures. The operating parameters were kept as 45 kV voltage, 45 mA current and a CuKa radiation source with 1.5418 Å wavelength. The obtained X-ray spectra were quantified *via* High Score Plus software. Scanning electron microscopy (SEM) was performed using a JEOL JSM-6480A for morphological analysis of synthesized materials at an operating voltage of 20 kV. In addition, the surface functionalization of the samples was investigated by Fourier transform infrared (FTIR) spectroscopy using a PerkinElmer's Spectrum 2 instrument. A concentration of 0.5 wt% of the samples was mixed with dried KBr for each sample measurement and the operating range was kept within 400 to 4000 $cm^{-1}$.

### 2.4 Electrochemical measurement

The electrochemical measurement for the HER was performed *via* a VERSASTAT4-500 containing a three electrode cell assembly. The cell assembly consists of a reference electrode (silver/silver chloride), counter electrode (Pt wire), working electrode (modified glassy carbon electrode (GCE)) and electrolyte (1.0 M KOH). The catalyst ink was used to modify the GCE. It consists of 5 mg as-synthesized catalyst, 30 μL of 5% Nafion solution and 5 mL DI water. Each catalyst ink was properly dispersed through an ultrasonic bath for 20 min. The obtained homogeneous ink was drop cast onto the cleaned surface of the GCE, and air was blown for drying. The dried GCE was placed into the cell assembly for electrochemical measurements.

HER polarization curves were obtained by linear sweep voltammetry (LSV) in 1.0 M KOH at a scan rate of 5 mV $s^{-1}$. The chrono-potentiometric test was used to determine the durability of the best sample at 10 mA $cm^{-2}$ and 20 mA $cm^{-2}$ current densities for 30 h. The electrochemical impedance spectroscopy (EIS) technique was performed for examination of the charge transfer resistance ($R_{ct}$) of various synthesized catalysts. It was operated at −0.4 V *vs.* RHE with 5 mV sinusoidal potential in the range of 100 000 Hz to 1 Hz frequency. Electrochemical active surface area (ECSA) of the samples was determined *via* the cyclic voltammetry (CV) technique, performed at various scan rates (30, 50, 70, 90, 110 and 130 mV $s^{-1}$) in the non-faradaic region. At last, the obtained potential data were converted into the reversible hydrogen electrode (RHE) through the Nernst equation:

$$E_{RHE} = E_{Ag/AgCl} + 0.059\ pH + E^{\circ}_{Ag/AgCl}$$

The $E_{Ag/AgCl}$ value is 0.197, while the overpotential ($\eta$) is calculated by subtracting the water splitting system's onset thermodynamic potential of 0 V for the HER.

$$\text{Overpotential } (\eta) = \text{onset potential } (E_{RHE})\ V - 0\ V$$

The Tafel formula has been employed to determine the Tafel slope.

$$\eta = b \log j + a$$

$\eta$ represents the overpotential, $b$ stands for the Tafel slope, $j$ denotes the current density, and $a$ represents the point of the intersection parameter or exchange current density.[38]

## 3. Results and discussion

### 3.1 Composition and structural analysis

Fig. 3 displays the distinct peak pattern of MAX powder ($Ti_3AlC_2$). It can be seen that the XRD patterns of pristine MAX powder has well-matched patterns with reference JCPDS no. 520-875 along with sharp and broader peaks at around 9.28°, 19.15°, 33.71°, 34.04°, 38.81°, 39.04°, 41.81°, 44.92°, 48.54°, 56.57° and 60.25° which correspond to the (002), (004), (100), (101), (008), (104), (105), (106), (107), (109) and (110) crystallographic planes.[39,40] The XRD diffraction pattern of MXenes

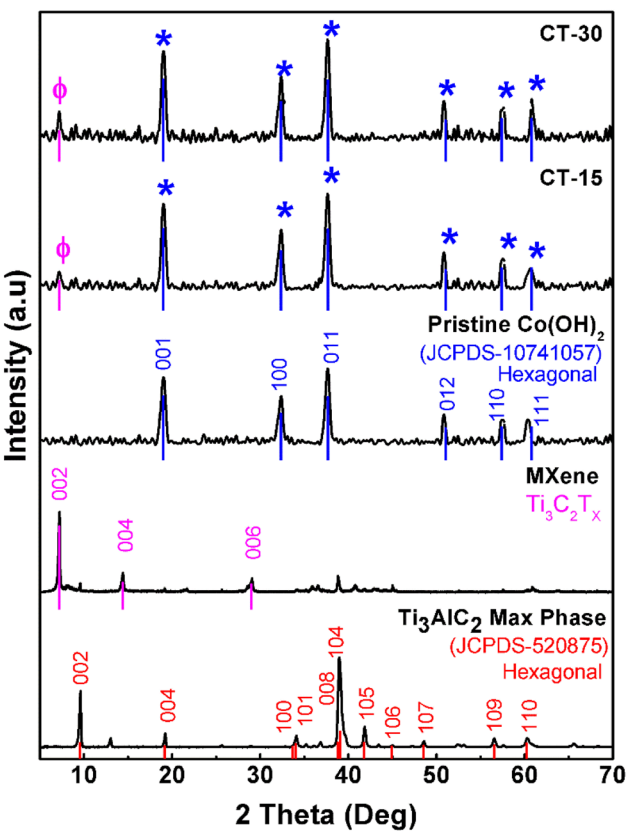


Fig. 3 XRD diffraction of $Ti_3AlC_2$(MAX), $Ti_3C_2T_x$ (MXene), $Co(OH)_2$, CT-15 and CT-30.

shows a major peak at 7.22° corresponding to the (002) plane and minor peaks at 14.4° and 29° which correspond to the (004) and (006) planes, also in good correlation with the literature.[41]

After HF + HCl exfoliation treatment, there was an impressive shift in the (002) peak from 2$\theta$ 9.26° to 7.22° suggesting the increase in the *c* lattice parameter. On the other hand, pristine $Co(OH)_2$ has broader peaks at 19.02°, 32.35°, 37.69°, 51.03°, 57.42° and 60.81° which correspond to the (001), (100), (011), (012), (11 0) and (111) crystallographic planes, which is well-matched with reference JCPDS no. 10741057 and with some reported research studies as well.[42,43] The MXene/$Co(OH)_2$ composite possessed nearly all the specific peaks of MXenes and $Co(OH)_2$, which confirmed the successful synthesis of the desired composite material. Besides, a little shift has been observed after composite formation, and this change may be attributed to the introduction of MXenes into $Co(OH)_2$ nanostructures as well as the variation of lattice parameters in the final crystal structure.[44]

The morphology and structural features of $Ti_3AlC_2$, exfoliated MXene, $Co(OH)_2$ and the composite CTs were studied by SEM analysis. The uneven surface and the closely packed structure of the MAX phase are shown in Fig. 4(a).[45] The exfoliated flake like morphology of MXenes was obtained after the HF + HCl treatment of the MAX phase (Fig. 4(b)).[46] Pristine $Co(OH)_2$ demonstrated an agglomerated spherical particle like morphology as shown in Fig. 4(c). However, composites (CT-15 and CT-30) show the growth of a spherical particle layer on MXene flakes as a combination of both structural features. Through SEM analysis (Fig. 4(d and e)), we have confirmed our successful synthesis of MXene integrated $Co(OH)_2$ materials based on the provided literature.[47]

The surface functionalization of synthesized materials has been conducted through FTIR spectroscopy. The FTIR spectra of $Ti_3AlC_2$ (MAX), $Ti_3C_2T_x$ (MXene), $Co(OH)_2$, CT-15 and CT-30 are shown in Fig. 5. It is observed that all materials revealed some common bands such as at 3438, 2930, 2854, 1601 and 1382 $cm^{-1}$ assigned to (O–H), (C–H), (C–H), (O–H) and (C–H),

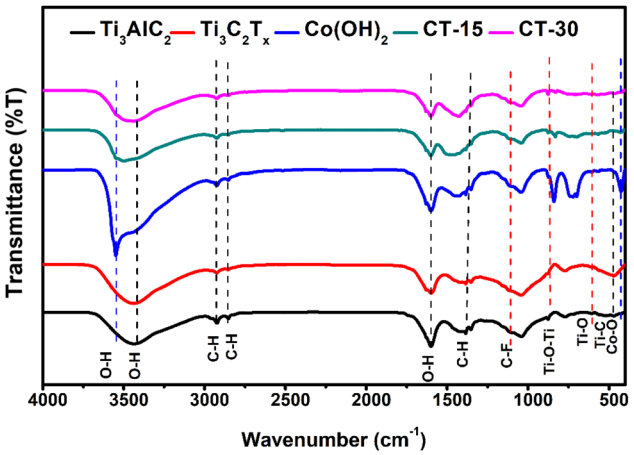


Fig. 5 FTIR spectra of $Ti_3AlC_2$ (MAX phase), $Ti_3C_2T_x$ (MXene), $Co(OH)_2$, CT-15 and CT-30.

respectively. The O–H groups are present due the absorption of external water $H_2O$ molecules on the surface of materials because of their hydrophilic nature. The presence of the C–H band in materials is attributed to symmetrical/asymmetrical methylene ($CH_2$) and methyl ($CH_3$) stretching.[46,48] Furthermore, the FTIR spectra of the $Ti_3AlC_2$ phase probably represent Ti–O–Ti and Ti–O deformation vibration linkage bonding at 879 and 605 $cm^{-1}$. Moreover, the peak at 481 $cm^{-1}$ represents the rocking or twisting vibration of Ti–C. However, the $Ti_3C_2T_x$ generated fluorine-terminated band (C–F) at 1108 $cm^{-1}$ and sharpness of the Ti–C band confirm the etching of the $Ti_3AlC_2$ MAX phase. The FTIR spectra of $Co(OH)_2$ showed the O–H and Co–O bands at 3540 and 425 $cm^{-1}$ which validate the formation of the cobalt hydroxide phase.[49,50] Despite of composite CT-15 and CT-30 exhibit the stretching and vibration band related to $Ti_3C_2T_x$ and $Co(OH)_2$ such as C–F, Ti–O–Ti, Ti–O–TiC, and Co–O bands.[51,52] It is also observed that the vibration band of Co–O is reduced with the addition of a higher amount of $Ti_3C_2T_x$ in CT-

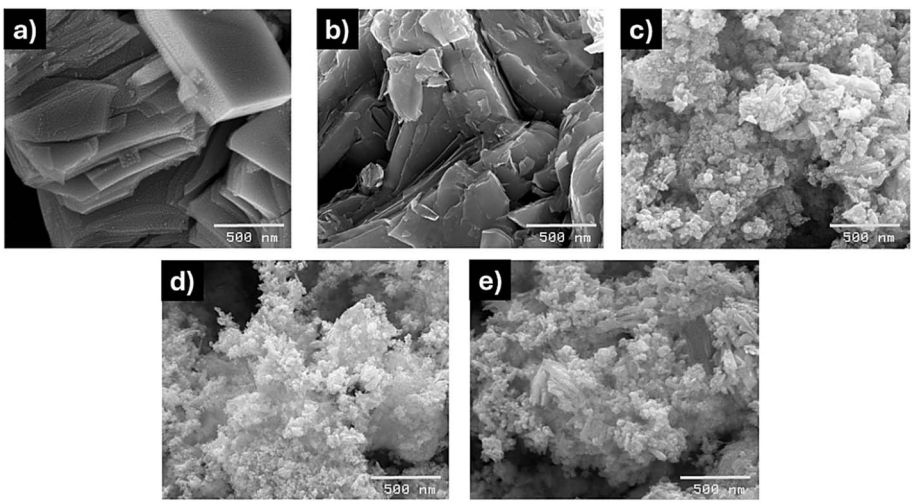


Fig. 4 SEM images: (a) $Ti_3AlC_2$ (MAX phase), (b) $Ti_3C_2T_x$ (MXene), (c) $Co(OH)_2$ and (d and e) CT-15 and CT-30.

30. Hence, this confirms the presence of $Ti_3C_2T_x$ in $Co(OH_2)$ nanostructures.

### 3.2 Electrochemical investigation

The electrochemical analysis was performed on $Ti_3AlC_2$, $Ti_3C_2T_x$, Co $(OH)_2$, CT-15 and CT-30 as shown in Fig. 6. These electrocatalysts were analysed for HER study through LSV in 1.0 KOH electrolyte, as presented in Fig. 6(a). The polarization curves reveal that $Ti_3AlC_2$ has an overpotential value of 676 mV whereas $Ti_3C_2T_x$ and Co $(OH)_2$ have shown lower overpotential values of 542 mV and 487 mV at a current density of 10 mA $cm^{-2}$. In contrast, CT-15 and CT-30 have shown much better HER activity compared to their counterparts with the overpotential values of 418 mV and 380 mV at a current density of 10 mA $cm^{-2}$, which is nearer to that of 20% Pt/C as a reference. The overpotential values corresponding to each catalyst can be observed *via* a histogram as shown in Fig. 6(b). According to comparative analysis with reported work mentioned in Table 1 this presented work is superior as compared to to previous reports. The relationship between the reaction rate and overpotential applied provides information about the electrochemical performance of electrocatalysts in terms of the Tafel slope which can be seen in Fig. 6(c). It is evident that CT-30 exhibits a Tafel slope value of 99 mV $dec^{-1}$, which is lower than the values observed for the other analysed samples, namely $Ti_3AlC_2$, $Ti_3C_2T_x$, $Co(OH)_2$, and CT-15, which have Tafel slope values of 214, 170, 147, and 112 mV $dec^{-1}$, respectively. In addition, 20% Pt/C has the lowest Tafel slope value of 37 mV $dec^{-1}$, which is nearer to that of CT-30 as compared to other as-prepared electrocatalysts. In an alkaline environment, the kinetics of the HER can be described by three sequential steps, as outlined in the equations.

$$H_2O + e^- + M \rightarrow MH_{ads} + OH^- \text{ (Volmer step)} \quad (1)$$

$$MH_{ads} + MH_{ads} \rightarrow H_2 + 2M \text{ (Tafel step)} \quad (2)$$

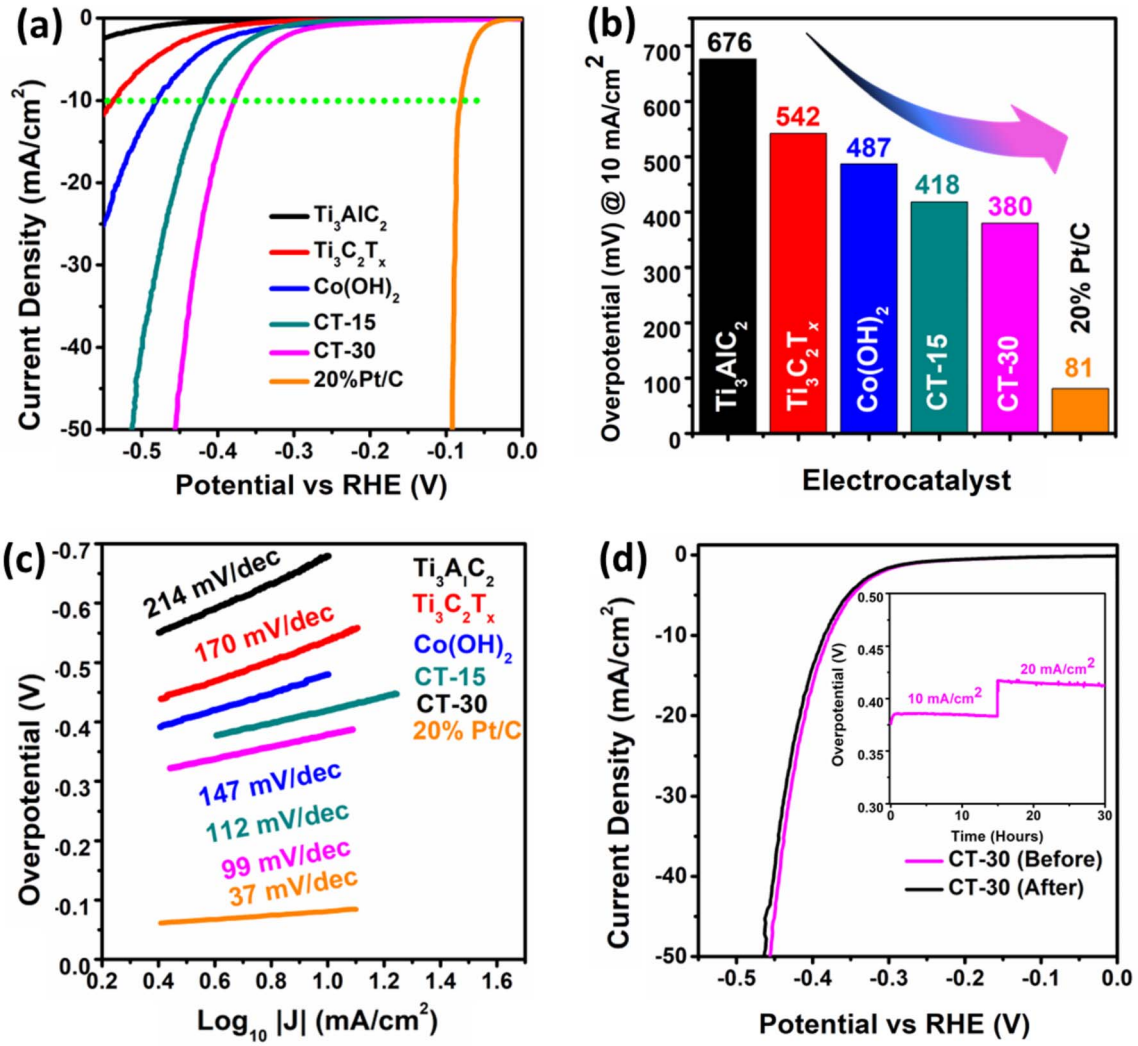


Fig. 6 (a) Linear Scan Voltammetry (LSV) of different catalysts with iR corrected data, (b) histogram representing overpotential of the prepared electrocatalysts, (c) corresponding Tafel slope values generated from LSV and (d) LSV measurement before and after the durability test; (inset) chronopotentiometric durability.

Table 1 Comparative analysis of the presented work with previous reported work

| Electrocatalyst | Electrolyte | Current density | Overpotential | Tafel slope | Ref. |
|---|---|---|---|---|---|
| **CT-30** | **1 M KOH** | **10 mA cm$^{-2}$** | **380 mV** | **99 mV dec$^{-1}$** | **This work** |
| $Fe_{50}Ni_{50}$ | 1 M NaOH | 10 mA cm$^{-2}$ | 390 mV | 96 mV dec$^{-1}$ | 53 |
| $MCO_3$ | 1 M KOH | 10 mA cm$^{-2}$ | 400 mV | 174 mV dec$^{-1}$ | 54 |
| $MoS_2/Ti_3C_2$ | 0.5 M $H_2SO_4$ | 10 mA cm$^{-2}$ | 400 mV | 74 mV dec$^{-1}$ | 55 |
| HC-$MoS_2/MoC_2$ | 1 M KOH | 1000 mA cm$^{-2}$ | 412 mV | 60 mV dec$^{-1}$ | 56 |
| BP Ir Sur | 1 M KOH | 10 mA cm$^{-2}$ | 420 mV | 50.4 mV dec$^{-1}$ | 57 |
| HF-MXene | 1 M KOH | 10 mA cm$^{-2}$ | 444 mV | 311 mV dec$^{-1}$ | 58 |
| N,P,O doped GC | 1 M KOH | 10 mA cm$^{-2}$ | 446 mV | 154 mV dec$^{-1}$ | 59 |
| Pt 3D Lig | 1 M KOH | 10 mA cm$^{-2}$ | 455 mV | 73.2 mV dec$^{-1}$ | 60 |
| Fe/Ni doped GO@MXene | 0.5 M $H_2SO$ | 10 mA cm$^{-2}$ | 470 mV | 110 mV dec$^{-1}$ | 34 |
| $Co^{3+}Ti_2CT_x$ | 1 M KOH | 10 | 460 | 103 | 61 |
| $Nb_4C_3T$ | 1 M KOH | 10 | 398 | 122 | 62 |

$$H_2O + MH_{ads} + e^- \rightarrow H_2 + M + OH^- \text{ (Heyrovsky step)} \quad (3)$$

According to eqn (1), the initial phase is associated with the Volmer step, which involves the adsorption of protons onto the surface of the electrode. Subsequently, the attached intermediate components merge, as illustrated in eqn (2) or the Heyrovsky step, which involves the absorption of the adsorbed substances as stated in eqn (3). $MH_{ads}$ is produced on the catalytically active site in the Volmer step as a result of reduction of the proton or $H_2O$.[63] There are two potential primary pathways to enter the second phase. The inclusion of two adsorbed hydrogen atoms ($MH_{ads}$) in the Tafel process could lead to the formation of $H_2$.[64] The Heyrovsky step represents another mechanism where $MH_{ads}$ could combine with a molecule of $H_2O$ and an extra electron to generate $H_2$. The most common approach to express the difficulty of initiating a reaction over a catalyst is by referring to the Gibbs free energy of hydrogen adsorption, typically abbreviated as ΔGH*, which quantifies the strength of the binding of H* to the surface of the electrocatalyst.[65] The Gibbs free energy of $H_2$ adsorption (ΔGH*) is commonly employed to assess the energy barrier associated with initiating a reaction on a catalyst. This parameter quantifies the extent of binding strength between $H_2$ species (H*) and the surface of the electrocatalyst. The suitability for the subject of interest is evident in the case of the HER, as the expected value of ΔGH* approaches zero, suggesting a state of equilibrium among the adsorption as well as desorption phenomena. The Heyrovsky step subsequently depicts the HER mechanism on the CT-30 composite.

The durability of the electrocatalyst CT-30 has also been conducted before and after the chronopotentiometry test Fig. 6(d). The stability of an electrocatalyst plays a pivotal role in real-time applications.[66] Hence, the CT-30 composite material has been examined for stability using chronopotentiometry at current densities of 10 and 20 mA cm$^{-2}$ over a duration of 30 h, thereby validating its long-term electrochemical performance. It is noteworthy that the proposed electrocatalyst has demonstrated stability, except for minor potential losses or fluctuations observed within the graph as shown in Fig. 6d (inset). The LSV polarization of CT-30 demonstrates that the electrocatalyst is well-stable in nature with some minor fluctuations in its curve.

The $R_{ct}$ of various electrocatalysts has been evaluated using EIS in a 1 M KOH medium. The Nyquist and Bode (I and II) plots are demonstrated in Fig. 7. Compared to $Ti_3AlC_2$, $Ti_3C_2T_x$, Co(OH)$_2$, and CT-15, the material CT-30 has exhibited an improved phase angle. Additionally, the $R_{ct}$ of $Ti_3AlC_2$, $Ti_3C_2T_x$, Co(OH)$_2$,

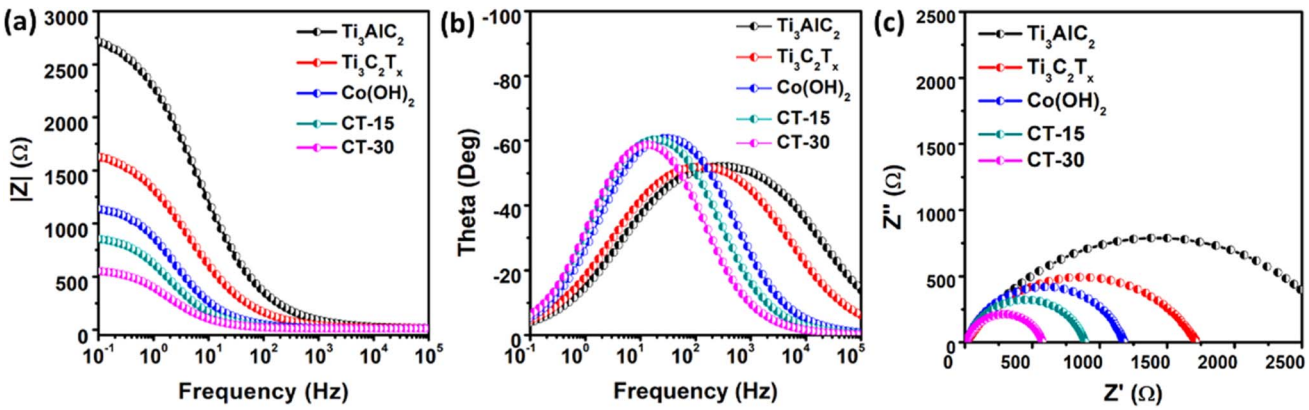


Fig. 7 Electrochemical impedance spectroscopy data of $Ti_3AlC_2$, $Ti_3C_2T_x$, Co(OH)$_2$, CT-15 and CT-30; (a & b) Bode plots (I and II); (c) Nyquist plot.

Table 2 Summarized HER based electrochemical features of the prepared catalysts

| | Calculated from LSV | | Calculated from EIS | | Calculated from CV | |
|---|---|---|---|---|---|---|
| | Overpotential | Tafel slope | Charge transfer resistance | Double layer capacitance | Double layer capacitance | Electrochemically active surface area |
| | $\eta_{10}$ | $B$ | $R_{ct}$ | $CPE_{dl}$ | $C_{dl}$ | ECSA |
| Catalyst | mV | mV dec$^{-1}$ | Ω | mF | μF cm$^{-2}$ | cm$^2$ |
| $Ti_3AlC_2$ | 676 | 214 | 2825 | 0.01 | 0.9 | 22.5 |
| $Ti_3C_2T_x$ | 542 | 170 | 1705 | 0.03 | 1.4 | 35 |
| $Co(OH)_2$ | 487 | 147 | 1167 | 0.08 | 4.8 | 120 |
| CT-15 | 418 | 112 | 878 | 0.13 | 5.4 | 135 |
| CT-30 | 380 | 99 | 563.1 | 0.22 | 9.2 | 230 |

CT-15, and CT-30 has been calculated to be 2825, 1705, 1167, 878, and 563.1 Ω. According to the data presented in Table 2 CT-30 has exhibited low $R_{ct}$ which indicates a higher electrical conductivity that provides better electrochemical performance as compared to its counterparts.

Furthermore, CV has also been utilized to investigate the double-layer capacitance ($C_{dl}$) within the non-faradaic region of the as-prepared materials as seen in Fig. 8(a–e). Various scan rates, including 30, 50, 70, 90, 110, and 130 mV s$^{-1}$, were employed for this analysis. Corresponding $C_{dl}$ values are calculated to be 0.9, 1.4, 4.8, 5.4, and 9.2 μF cm$^{-2}$ for $Ti_3AlC_2$, $Ti_3C_2T_x$, Co $(OH)_2$, CT-15, and CT-30, respectively (Fig. 8(f)). Moreover, the electrochemical active surface area (ECSA) has been calculated through $C_{dl}$ values through the given formula:

$$\text{ECSA} = \frac{C_{dl}}{C_s} \quad (4)$$

In the given expression (4), $C_{dl}$ represents the double-layer capacitance, while $C_s$ is regarded as the specific capacitance at the electrolyte interface. Notably, the value of $C_s$ is 0.04 mF cm$^{-2}$ for KOH. The corresponding values of ECSA for $Ti_3AlC_2$,

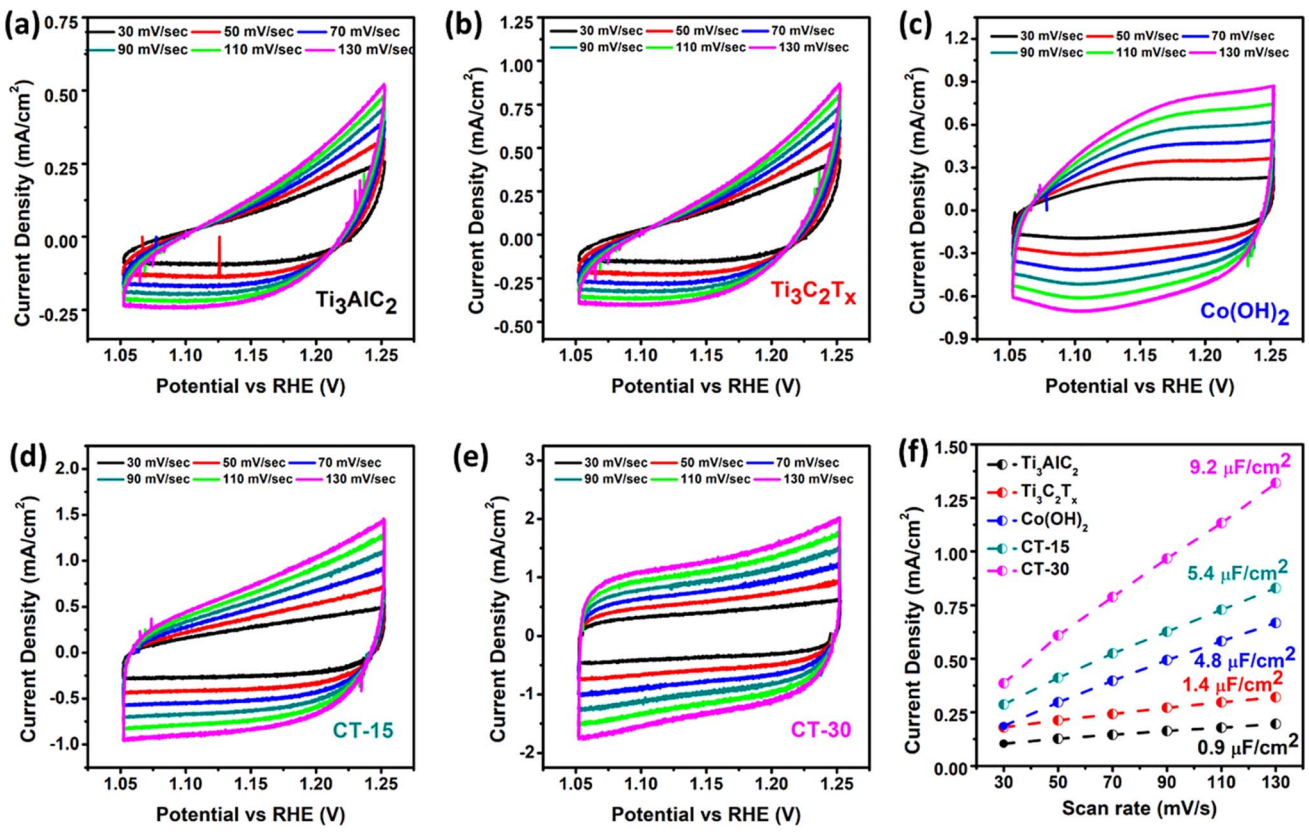


Fig. 8 Cyclic voltammetry data (a–e) of $Ti_3AlC_2$, $Ti_3C_2T_x$, $Co(OH)_2$, CT-15 and CT-30 and (f) double layer capacitance data of the prepared catalyst extracted from CV data.

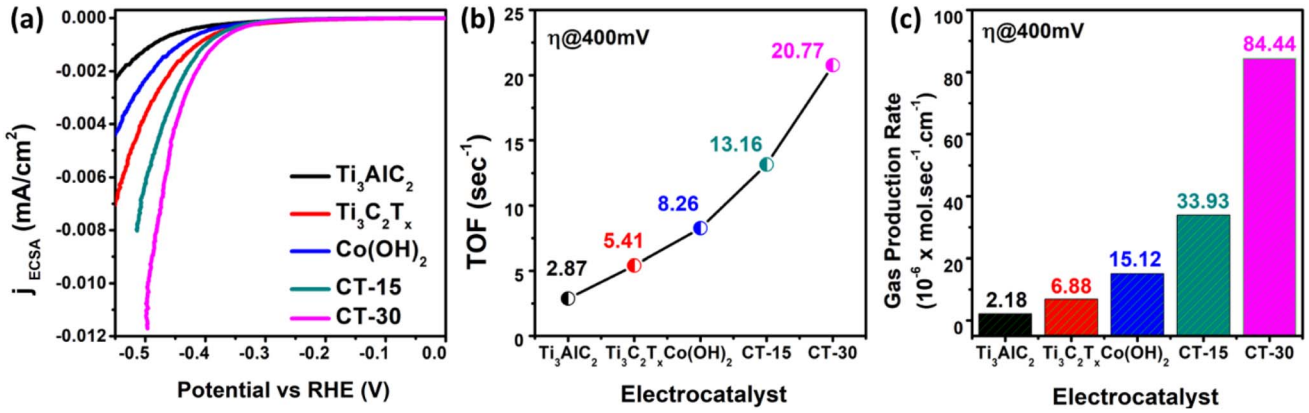


Fig. 9 (a) ECSA normalized LSV curve, (b) TOFs at 400 mV overpotential and (c) theoretical gas production rate at a fixed overpotential of 400 mV of various catalysts.

$Ti_3C_2T_x$, Co $(OH)_2$, CT-15, and CT-30 have been calculated to be 22.5, 35, 120, 135, and 230 cm$^2$. The higher ECSA value of CT-30 may be attributed to the synergistic effect of two distinct materials with more active sites.[67]

The LSV polarization data are normalized *via* ECSA to minimize the effect of electrochemical surface area on the HER activity as shown in Fig. 9(a). The normalized curve of CT-30 shows superior HER performance as compared to CT-15, Co $(OH)_2$, $Ti_3C_2T_x$, and $Ti_3AlC_2$. It is revealed that CT-30 has improved intrinsic activity. Furthermore, the turnover frequency (TOF) is also determined for assessing the actual performance of the prepared catalyst using the following formula.

$$\mathrm{TOF} = \frac{j \times A}{n \times F \times m} \quad (5)$$

In the above eqn (5), TOF is the turnover frequency (s$^{-1}$), $j$ represents the current density obtained at a specific overpotential, $A$ is the electrode area, $n$ is the number of electrons in the reaction, $F$ represents the Faraday constant, and $m$ denotes the number of moles of the active deposited material. The TOF of various electrocatalysts is calculated at a fixed overpotential of 400 mV as given in Fig. 9(b). The current densities and corresponding TOFs of $Ti_3AlC_2$, $Ti_3C_2T_x$, Co $(OH)_2$, CT-15, and CT-30 are (0.42 mA cm$^{-2}$ and 2.87 s$^{-1}$), (1.32 mA cm$^{-2}$ and 5.41 s$^{-1}$), (2.91 mA cm$^{-2}$ and 8.26 s$^{-1}$), (6.54 mA cm$^{-2}$ and 13.16 s$^{-1}$) and (16.30 mA cm$^{-2}$ and 20.77 s$^{-1}$) respectively. It can be suggested that CT-30 can significantly outperform in industrial applications. Due to this fact, theoretical hydrogen production is also determined to validate the gas production rate of the electrocatalyst. The theoretical gas production is calculated using the given equation.

$$r = \frac{i}{nF} \quad (6)$$

Here, in eqn (6), $r$ is the gas production rate (mol s$^{-1}$ cm$^{-1}$), $i$ is the recorded current density at a specific overpotential, $n$ is the electron transfer number ($n$ = 2 in the HER), and $F$ is the Faraday constant (96 485.3 s A mol$^{-1}$). The hydrogen gas production rate of various catalysts can be seen in Fig. 9(c). The result revealed that CT-30 has a higher hydrogen production rate *i.e.*, 84.44 × 10$^{-6}$ mol s$^{-1}$ cm$^{-1}$ as compared to others. Such an improvement could have enhanced the performance of this composition, making it promising for HER activity in KOH media. Various electrochemical characteristic features of as-prepared materials are illustrated in Table 2. Conclusively, the material CT-30 exhibited robust electrochemical performance and has been compared with recent studies.

## 4. Conclusion

In summary, the presented electrocatalysts were effectively prepared by the aqueous chemical growth method. The 2D layered MXene $T_3C_2T_x$ was introduced into the matrix of cobalt hydroxide $Co(OH)_2$ nanostructures for the preparation of their composites. The physicochemical characteristics of the as-synthesized composites along with their pristine samples were analysed *via* various analytical techniques. X-ray diffraction (XRD) and Fourier transform infrared spectroscopy (FTIR) analyses were carried out to confirm the successful preparation of the as-prepared samples including pristine $Ti_3AlC_2$, $Ti_3C_2T_x$, Co $(OH)_2$ samples, and CT-15, and CT-30 composites. Scanning electron microscopy (SEM) was also carried out for all as-prepared samples to confirm their morphology. Composite CT-30 shows the lowest overpotential of 380 mV at 10 mA cm$^{-2}$ current density, among pristine samples and other composites in alkaline electrolyte. In addition, the low Tafel value of CT-30 of about 99 mV dec$^{-1}$ further optimized HER activity. It is perceived that the CT-30 catalyst is durable and stable at 10 mA cm$^{-2}$ and 20 mA cm$^{-2}$ current densities for 30 h without any major drop in the potential value. A low charge transfer resistance ($R_{ct}$) of 563.1 Ω, higher double layer capacitance ($C_{dl}$) value of 9.2 μF cm$^{-2}$ and greater electrochemical active surface area (ECSA) of 230 cm$^2$ are achieved because the thin layered structure of $Ti_3C_2T_x$ facilitates easy transport of charges into $Co(OH)_2$ nanostructures. Hence, it enhances the robustness of the HER that is beneficial for energy production and storage applications for sustainable society.

## Data availability

The data will be available on request.

## Conflicts of interest

The authors of this paper have acknowledged no conflicts of interest.

## Acknowledgements

The authors would like to acknowledge the Researcher's Supporting Project Number (RSP2024R269) King Saud University, Riyadh, Saudi Arabia.

## References

1 R. Badrnezhad and et al, ., Effect of iron on Ni–Mo–Fe composite as a low-cost bifunctional electrocatalyst for overall water splitting, *Int. J. Hydrogen Energy*, 2021, **46**(5), 3821–3832.
2 Y. Xiao, Nanoclusters for photoelectrochemical water splitting: bridging the photosensitizer and carrier transporter, *EcoEnergy*, 2023, **1**(1), 60–84.
3 J. Ren and et al, ., Modulating amorphous/crystalline heterogeneous interface in $RuCoMo_yO_x$ grown on nickel foam to achieve efficient overall water splitting, *Chem. Eng. J.*, 2023, **469**, 143993.
4 U. Aftab, *et al.*, Mixed $CoS_2$@$Co_3O_4$ composite material: an efficient nonprecious electrocatalyst for hydrogen evolution reaction, *Int. J. Hydrogen Energy*, 2020, **45**(27), 13805–13813.
5 A. Hanan, *et al.*, $Co_2FeO_4$@rGO composite: towards trifunctional water splitting in alkaline media, *Int. J. Hydrogen Energy*, 2022, **47**(80), 33919–33937.
6 A. Pareek, *et al.*, Insights into renewable hydrogen energy: recent advances and prospects, *Mater. Sci. Energy Technol.*, 2020, **3**, 319–327.
7 A. J. Laghari and et al, ., MgO as promoter for electrocatalytic activities of $Co_3O_4$–MgO composite *via* abundant oxygen vacancies and $Co^{2+}$ ions towards oxygen evolution reaction, *Int. J. Hydrogen Energy*, 2023, **48**(34), 12672–12682.
8 P. Banoth, C. Kandula and P. Kollu, Introduction to Electrocatalysts, in *Noble Metal-free Electrocatalysts: New Trends in Electrocatalysts for Energy Applications*, American Chemical Society, 2022, vol. 2, p. 1–37.
9 Z. H. Ibupoto, $NiCo_2O_4$ nanostructures loaded onto pencil graphite rod: an advanced composite material for oxygen evolution reaction, *Int. J. Hydrogen Energy*, 2022, **47**(10), 6650–6665.
10 J. Liu, V-Doping Strategy Induces the Construction of the Functionally Complementary $Ru_2P$/V-$RuP_4$ Heterostructures to Achieve Amperometric Current Density for HER, *Adv. Funct. Mater.*, 2024, **34**(28), 2315773.
11 W. Li and et al, ., Defective $RuO_2$/$TiO_2$ nano-heterostructure advances hydrogen production by electrochemical water splitting, *Chem. Eng. J.*, 2022, **431**, 134072.
12 Y. Du, Recent advances in interface engineering strategy for highly-efficient electrocatalytic water splitting, *InfoMat*, 2023, **5**(1), e12377.
13 N. T. T. Thao, Current Trends of Iridium-Based Catalysts for Oxygen Evolution Reaction in Acidic Water Electrolysis, *Small Sci.*, 2024, **4**(1), 2300109.
14 A. Das, *et al.*, Zinc doping induced $WS_2$ accelerating the HER and ORR kinetics: a theoretical and, *Catal. Today*, 2023, **423**, 113921.
15 M. Smialkowski and et al, ., Trimetallic Pentlandites $(Fe,Co,Ni)_9S_8$ for the Electrocatalytical HER in Acidic Media, *ACS Mater. Au*, 2022, **2**(4), 474–481.
16 Y. J. Bai and et al, ., Tunable and Specific Formation of C@NiCoP Peapods with Enhanced HER Activity and Lithium Storage Performance, *Chem.–Eur. J.*, 2016, **22**(3), 1021–1029.
17 B. T. Jebaslinhepzybai and et al, ., One-pot solvothermal synthesis of $Co_2P$ nanoparticles: an efficient HER and OER electrocatalysts, *Int. J. Hydrogen Energy*, 2021, **46**(42), 21924–21938.
18 C. J. Rupp, J. Anversa and R. J. Baierle, First principles of Si-doped $BC_2N$ single layer for hydrogen evolution reaction (HER), *Int. J. Hydrogen Energy*, 2023, **48**(20), 7294–7304.
19 J. Verma and S. Goel, Cost-effective electrocatalysts for Hydrogen Evolution Reactions (HER): Challenges and Prospects, *Int. J. Hydrogen Energy*, 2022, **47**(92), 38964–38982.
20 T. T. Wang and et al, ., Nanoframes of $Co_3O_4$-$Mo_2N$ Heterointerfaces Enable High-Performance Bifunctionality toward Both Electrocatalytic HER and OER, *Adv. Funct. Mater.*, 2022, **32**(7), 2107382.
21 S. T. Huang and et al, ., Ru-promoted NiFe oxyhydroxide anchored on the hierarchical porous N-doped carbon aerogel: electronic structures modulation for much enhanced OER/HER dual-functional characteristics, *Appl. Catal., A*, 2023, **664**, 119331.
22 S. N. Lin and et al, ., The Mechanism of One-Step Synthesis of Oxides from Metal Chlorides and Their Electrocatalytic HER Study, *Cryst. Res. Technol.*, 2022, **57**(8), 2200008.
23 H. H. Do and et al, ., Cobalt compounds-based hollow structure electrocatalysts for water splitting: a review, *Int. J. Hydrogen Energy*, 2024, **49**, 613–632.
24 X.-Y. Zhang and et al, ., Amorphous-crystalline catalytic interface of CoFeOH/CoFeP with double sites based on ultrafast hydrolysis for hydrogen evolution at high current density, *J. Power Sources*, 2021, **507**, 230279.
25 X. Feng and et al, ., Construction of hierarchical nickel/cobalt iron-hydroxide and nickel/cobalt selenide nanotubes for efficient electrocatalytic water splitting, *New J. Chem.*, 2020, **44**(18), 7552–7560.
26 W. Peng and et al, Ru and Se Co-Doped Cobalt Hydroxide Electrocatalyst for Efficient Hydrogen Evolution Reactions, *Molecules*, 2023, **28**(15), 5736.
27 A. Hanan and et al, ., MXenes and heterostructures-based electrocatalysts for hydrogen evolution reaction: recent developments and future outlook, *J. Energy Chem.*, 2024, **92**, 176–206.

28 M. Rahman and M. S. Al Mamun, Future prospects of MXenes: synthesis, functionalization, properties, and application in field effect transistors, *Nanoscale Adv.*, 2024, **6**(2), 367–385.

29 S. B. Devi and R. Navamathavan, One-Pot Hydrothermal Synthesis of $Ti_3C_2$ (MXene)-$CoS_2$ Nanocomposite as a Bifunctional Electrocatalyst (HER/OER) for a Clean Environment, *J. Electrochem. Soc.*, 2023, **170**(9), 096503.

30 D. Liu and et al, ., Nitrogen-Doped $MoS_2/Ti_3C_2T_x$ Heterostructures as Ultra-Efficient Alkaline HER Electrocatalysts, *Inorg. Chem.*, 2021, **60**(13), 9932–9940.

31 L. P. Hao, Synergistic Integration of MXene and Metal-Organic Frameworks for Enhanced Electrocatalytic Hydrogen Evolution in an Alkaline Environment, *Catalysts*, 2023, **13**(5), 802.

32 N. H. Attanayake and et al, ., Vertically aligned $MoS_2$ on $Ti_3C_2$ (MXene) as an improved HER catalyst, *J. Mater. Chem. A*, 2018, **6**(35), 16882–16889.

33 J. Y. Loh, F. M. Yap and W. J. Ong, 2D/2D heterojunction interface: Engineering of 1T/2H $MoS_2$ coupled with $Ti_3C_2T_x$ heterostructured electrocatalysts for pH-universal hydrogen evolution, *J. Mater. Sci. Technol.*, 2024, **179**, 86–97.

34 S. K. Raj and et al, ., Three-dimensional Ni/Fe doped graphene oxide@MXene architecture as an efficient water splitting electrocatalyst, *Int. J. Hydrogen Energy*, 2022, **47**(99), 41772–41782.

35 Z. Z. Xu and et al, ., Facile fabrication of carbon fiber skeleton structure of $MoS_2$ supported on 2D MXene composite with highly efficient and stable hydrogen evolution reaction, *Compos. Sci. Technol.*, 2022, 222.

36 L. Ma and et al, ., CoP nanoparticles deposited on reduced graphene oxide sheets as an active electrocatalyst for the hydrogen evolution reaction, *J. Mater. Chem. A*, 2015, **3**(10), 5337–5343.

37 T. A. Le, *et al.*, Porosity-Engineering of MXene as a Support Material for a Highly Efficient Electrocatalyst toward Overall Water Splitting, *ChemSusChem*, 2020, **13**(5), 945–955.

38 M. Y. Solangi and et al, ., In-situ growth of nonstoichiometric $CrO_{0.87}$ and $Co_3O_4$ hybrid system for the enhanced electrocatalytic water splitting in alkaline media, *Int. J. Hydrogen Energy*, 2023, 36439–36451.

39 Z. Mahmoudi, *et al.*, Synthesis of $Ti_2AlC$ & $Ti_3AlC_2$ MAX phases by Arc-PVD using Ti–Al target in $C_2H_2$/Ar gas mixture and subsequent annealing, *Ceram. Int.*, 2020, **46**(4), 4968–4975.

40 V. I. Vershinnikov and D. Y. Kovalev, Preparation of $Ti_2AlC$ and $Ti_3AlC_2$ MAX Phases by Self-Propagating High-Temperature Synthesis with the Reduction Stage, *Russ. J. Non-Ferrous Metals*, 2020, **61**(5), 554–558.

41 R. R. Raja Sulaiman, Structurally modified MXenes-based catalysts for application in hydrogen evolution reaction: a review, *Catalysts*, 2022, **12**(12), 1576.

42 J. Zhu and et al, ., Composites of $TiO_2$ Nanoparticles Deposited on $Ti_3C_2$ MXene Nanosheets with Enhanced Electrochemical Performance, *J. Electrochem. Soc.*, 2016, **163**(5), A785.

43 A. Tariq and et al, ., Efficient Visible-Light Photocatalysis of 2D-MXene Nanohybrids with $Gd^{3+}$- and $Sn^{4+}$-Codoped Bismuth Ferrite, *ACS Omega*, 2018, **3**(10), 13828–13836.

44 M. Mahmood and et al, ., Synthesis of Ultrathin $MnO_2$ Nanowire-Intercalated 2D-MXenes for High-Performance Hybrid Supercapacitors, *Energy Fuels*, 2021, **35**(4), 3469–3478.

45 S. Munir and et al, ., Exploring the Influence of Critical Parameters for the Effective Synthesis of High-Quality 2D MXene, *ACS Omega*, 2020, **5**(41), 26845–26854.

46 X. Li and et al, ., Advances in MXene Films: Synthesis, Assembly, and Applications, *Trans. Tianjin Univ.*, 2021, **27**(3), 217–247.

47 A. Sunny, S. Rajalekshmi and A. Pandikumar, Nanocomposite engineering: Tailoring MXene/Cobalt oxide for efficient electrocatalytic hydrogen and oxygen evolution reactions, *J. Alloys Compd.*, 2024, **1003**, 175532.

48 N. U. Kiran and et al, ., Comparative Study of Cold Electron Emission from 2D $Ti_3C_2T_x$ MXene Nanosheets with Respect to Its Precursor $Ti_3SiC_2$ MAX Phase, *ACS Appl. Electron. Mater.*, 2022, **4**(6), 2656–2666.

49 J. Wang and et al, ., Fabrication of dispersive $\alpha$-$Co(OH)_2$ nanosheets on graphene nanoribbons for boosting their oxygen evolution performance, *J. Mater. Sci.*, 2019, **54**(10), 7692–7701.

50 M. R. da Silva Pelissari and et al, ., Ascorbic acid electrocatalytic activity in different electrolyte solutions using electrodeposited $Co(OH)_2$, *Ionics*, 2019, **25**(4), 1911–1920.

51 D. Liu and et al, ., Magnetic $Ti_3C_2$ MXene Nanomaterials for Doxorubicin Adsorption from Aqueous Solutions: Kinetic, Isotherms, and Thermodynamic Studies, *ACS Omega*, 2022, **7**(36), 31945–31953.

52 L. Pu and et al, ., N-doped MXene derived from chitosan for the highly effective electrochemical properties as supercapacitor, *Adv. Compos. Hybrid Mater.*, 2022, **5**(1), 356–369.

53 S. I. Perez Bakovic and et al, ., Electrochemically active surface area controls HER activity for $Fe_xNi_{100-x}$ films in alkaline electrolyte, *J. Catal.*, 2021, **394**, 104–112.

54 S. Maitra and et al, ., Electrochemical aspects of sol-gel synthesized $MgCoO_2$ for aqueous supercapacitor and alkaline HER electrocatalyst applications, *Curr. Appl. Phys.*, 2020, **20**(12), 1404–1415.

55 L. Huang and et al, ., Hierarchical $MoS_2$ nanosheets integrated $Ti_3C_2$ MXenes for electrocatalytic hydrogen evolution, *Int. J. Hydrogen Energy*, 2019, **44**(2), 965–976.

56 C. Zhang and et al, ., High-throughput production of cheap mineral-based two-dimensional electrocatalysts for high-current-density hydrogen evolution, *Nat. Commun.*, 2020, **11**(1), 3724.

57 J. Mei, Surface-Dependent Intermediate Adsorption Modulation on Iridium-Modified Black Phosphorus Electrocatalysts for Efficient pH-Universal Water Splitting, *Adv. Mater.*, 2021, **33**(49), 2104638.

58 B. Sarfraz, HF free greener Cl-terminated MXene as novel electrocatalyst for overall water splitting in alkaline media, *Int. J. Energy Res.*, 2022, **46**(8), 10942–10954.
59 J. Zhang, Carbon-Rich Nanomaterials: Fascinating Hydrogen and Oxygen Electrocatalysts, *Adv. Mater.*, 2018, **30**(40), 1800528.
60 I. Khan and et al, ., Robust electrocatalysts decorated three-dimensional laser-induced graphene for selective alkaline OER and HER, *Carbon*, 2023, **213**, 118292.
61 S.-Y. Pang and et al, ., Universal Strategy for HF-Free Facile and Rapid Synthesis of Two-dimensional MXenes as Multifunctional Energy Materials, *J. Am. Chem. Soc.*, 2019, **141**(24), 9610–9616.
62 Y. Tan and et al, ., $Nb_4C_3T_x$ (MXene) as a new stable catalyst for the hydrogen evolution reaction, *Int. J. Hydrogen Energy*, 2021, **46**(2), 1955–1966.
63 S. Tang and et al, ., Recent advances in transition metal nitrides for hydrogen electrocatalysis in alkaline media: from catalyst design to application, *Front. Chem.*, 2022, **10**, 1073175.
64 S. Pakhira, V. Kumar and S. Ghosh, Revealing the Superior Electrocatalytic Performance of 2D Monolayer $WSe_2$ Transition Metal Dichalcogenide for Efficient H2 Evolution Reaction, *Adv. Mater. Interfaces*, 2023, **10**(8), 2202075.
65 A. Kazemi, F. Manteghi and Z. Tehrani, Metal Electrocatalysts for Hydrogen Production in Water Splitting, *ACS Omega*, 2024, **9**(7), 7310–7335.
66 R. A. Mir, S. Upadhyay and O. P. Pandey, A review on recent advances and progress in $Mo_2C$@C: a suitable and stable electrocatalyst for HER, *Int. J. Hydrogen Energy*, 2023, **48**(35), 13044–13067.
67 S. Venkateshalu and et al, ., Synergistic MXene/LDH heterostructures with extensive interfacing as emerging energy conversion and storage materials, *J. Mater. Chem. A*, 2023, **11**(27), 14469–14488.